

Novel Morphologic and Genetic Analysis of Cancer Cells in a 3D Microenvironment Identifies STAT3 as a Regulator of Tumor Permeability Barrier Function

Min Chul Park^{1,2}, Hyobin Jeong³, Sung Hwa Son¹, YounHa Kim^{1,4}, Daeyoung Han^{1,4}, Peter C. Goughnour^{1,4}, Taehee Kang¹, Nam Hoon Kwon¹, Hyo Eun Moon⁵, Sun Ha Paek⁵, Daehee Hwang^{3,6}, Ho Jun Seol⁷, Do-Hyun Nam⁷, and Sunghoon Kim^{1,4,8}

Abstract

Tumor permeability is a critical determinant of drug delivery and sensitivity, but systematic methods to identify factors that perform permeability barrier functions in the tumor microenvironment are not yet available. Multicellular tumor spheroids have become tractable *in vitro* models to study the impact of a three-dimensional (3D) environment on cellular behavior. In this study, we characterized the spheroid-forming potential of cancer cells and correlated the resulting spheroid morphologies with genetic information to identify conserved cellular processes associated with spheroid structure. Spheroids generated from 100 different cancer cell lines were classified into four distinct groups based on morphology. In particular, round and compact spheroids exhibited highly hypoxic inner cores and permeability barriers against anticancer drugs. Through

systematic and correlative analysis, we reveal JAK–STAT signaling as one of the signature pathways activated in round spheroids. Accordingly, STAT3 inhibition in spheroids generated from the established cancer cells and primary glioblastoma patient-derived cells altered the rounded morphology and increased drug sensitivity. Furthermore, combined administration of the STAT3 inhibitor and 5-fluorouracil to a mouse xenograft model markedly reduced tumor growth compared with monotherapy. Collectively, our findings demonstrate the ability to integrate 3D culture and genetic profiling to determine the factors underlying the integrity of the permeability barrier in the tumor microenvironment, and may help to identify and exploit novel mechanisms of drug resistance. *Cancer Res*; 76(5); 1044–54. ©2015 AACR.

Introduction

The hyperproliferation of cancer cells can generate tight cell–cell and cell–extracellular matrix interactions that are responsible for permeability barrier to oxygen, nutrition, and drug (1, 2). As this microenvironment would affect cancer cell growth and drug resistance (3–5), it is important to identify the factors

critical for permeability barrier. However, the methods to evaluate the physical characteristics of tumors are limited. The classical two-dimensional (2D) cell culture system is not appropriate as it does not well reflect the architecture of tumors *in vivo*. Although animal models can be used, they are time consuming, difficult to control, and inconvenient to monitor physical environment of tumors (6).

As tumor morphology is predominantly determined by cell–cell and cell–extracellular matrix interactions (7, 8) involving adhesion molecules and receptors (9, 10), the morphology and architecture of solid tumors is better reflected in three-dimensional (3D) culture than in monolayer culture (11, 12). The classical 3D culture model is multicellular spheroids, which are formed by self-assembly induced by cell–cell and cell–matrix interactions. Multicellular spheroids possess architecture resembling the structural and functional features of tumor tissue (12). For example, conditions of hypoxia and low nutrient concentration are generated in their core regions because of limited diffusion of oxygen and nutrients to their interiors (13, 14). In addition, heterogeneous cell populations are spontaneously induced in cancer spheroids by nutrient gradients (15). Adapting to metabolic insufficiency, the core cells of spheroid become quiescent and resistant to apoptosis (16, 17). Because of their tumor tissue–like characteristics, tumor spheroids have become increasingly attractive models to investigate cancer pathophysiology and develop antitumor therapeutics (18). In this work, we have employed the structural characteristics of tumor spheroids

¹Medicinal Bioconvergence Research Center, Seoul National University, Seoul, Korea. ²Advanced Institutes of Convergence Technology, Seoul National University, Suwon, Korea. ³School of Interdisciplinary Bioscience and Bioengineering, POSTECH, Pohang, Korea. ⁴Department of Molecular Medicine and Biopharmaceutical Sciences, Graduate School of Convergence Technology, College of Pharmacy, Seoul National University, Seoul, Korea. ⁵Department of Neurosurgery, Cancer Research Institute, Seoul National University College of Medicine, Seoul, Korea. ⁶Center for Systems Biology of Plant Senescence and Life History, Institute for Basic Science, Department of New Biology, DGIST, Daegu, Korea. ⁷Department of Neurosurgery, Samsung Medical Center, School of Medicine, Sungkyunkwan University, Seoul, Korea. ⁸The National Center for Drug Screening, Shanghai Institute of Materia Medica, Chinese Academy of Sciences, Shanghai, China.

Note: Supplementary data for this article are available at Cancer Research Online (<http://cancerres.aacrjournals.org/>).

Corresponding Author: Sunghoon Kim, Medicinal Bioconvergence Research Center, Seoul National University, Gwanak-ro 599, Gwanak-gu, Seoul 151-742, Korea. Phone: 822-880-8180; Fax: 822-875-2621; E-mail: sungkim@snu.ac.kr

doi: 10.1158/0008-5472.CAN-14-2611

©2015 American Association for Cancer Research.

and genetic profiles of cancer cells to identify signal pathways that could be implicated for the determination of tumor permeability and selected STAT3 as a target for further in-depth studies. We validated its significance for the determination of tumor permeability using cancer patient-derived primary cells and *in vivo* tumor model.

Materials and Methods

Cell culture

PC14PE6 and PC14PE6_LvBr3 cells were provided by Dr. Do-Hyun Nam (Samsung Medical Center, Seoul, Korea). D54, LN428, LN751, U251E4, and U87E4 cells were provided by Dr. W.K. Alfred Yung (MD Anderson Cancer Center, Houston, TX). SN-12C, SNU-119, SNU-216, SNU-668, SNU-719, HCC-1171, HCC-1195, HCC-15, HCC-1588, HCC-2108, and HCC-44 cell lines were obtained from Korean Cell Line Bank, and the others cell lines were obtained from ATCC. All cell lines, obtained 2 years ago, were authenticated by SNP fingerprinting and used within 20 passages. Cells were cultured in 10% FBS-containing media, including DMEM, RPMI1640, Minimum Essential Medium, and Eagle Minimum Essential Medium (Hyclone).

GBM patient-derived primary cell culture

Glioblastoma multiforme (GBM) patient-derived primary cell clones were obtained from GBM patients who had brain surgery at the Samsung Medical Center (Seoul, Korea) in accordance with the appropriate Institutional Review Boards. Dissociated GBM cells were cultured on the laminin (Sigma-Aldrich)-coated flasks. GBM patient-derived primary cells were cultured in neurobasal media with N2 and B27 supplements (0.5 \times , Invitrogen) and human recombinant basic fibroblast growth factor and EGF (25 ng/mL, R&D Systems; refs. 19, 20). Genetic profiles were used to select molecular signatures, contributing to the separation of the spheroid types. The GEO accession numbers for the gene expression and comparative genomic hybridization data used in this article are GSE42670 and GSE58401.

3D cell culture

The 2D cultured cells prior to the third passage were dissociated to single cells by Accumax (Millipore) and seeded to Lipidure-coated 3D culture plate (NOF Corporation). Spheroid morphology was monitored by bright-field function of fluorescence microscopy (Nikon C1). Live images of spheroid formation were acquired in 10-minute interval snapshots. These images were taken in 5% CO₂ incubator by using the bright-field function of Juli smart fluorescence cell analyzer (Digital Bio Technology) equipped with a 10 \times objective lens for 36 hours. The growth rate was determined by counting the spheroid cell number at the indicated day. Spheroids (2,000 cells seeded per well) were incubated with Accumax for 30 minutes to get single cells. The number of dissociated single cells was counted with disposable hemocytometer C-Chip (INCYTO).

Hypoxia assay

The hypoxic region inside the spheroid was detected by the hypoxia probe, LOX-1 (Scivax), as described previously (21). Briefly, the spheroid was cultured for 5 or 6 days and then treated with 2 μ mol/L LOX-1 for 24 hours. Red-phosphorescence was

measured by fluorescence microscopy electron multiplying charge-coupled device (EMCCD; Nikon C1).

Statistical analysis

Statistical analysis was performed using the ANOVA for multiple groups and unpaired, two-tailed, Student *t* test as indicated in figure legends. All results are presented as means \pm SEM. *P* < 0.05 was considered statistically significant. Each experiment was repeated independently at least three times.

Additional details are provided in the Supplementary Materials and Methods.

Results

Validation of multicellular cancer spheroid

To generate tumor spheroids, we used a low-attachment plate that was coated with 2-methacryloyloxy ethyl phosphorylcholine (MPC). As MPC has the same structure as phosphatidylcholine polar bases of cell membrane, it simulates human cell membrane-like surface (22). Cancer cells were first cultured in 2D culture plate to generate sufficient cell numbers. After two rounds of subculture, the cells were transferred to the 3D culture plate to induce spheroid formation. After spheroid formation, the medium was changed every 3 days and the spheroids were monitored for 1 to 4 weeks. We validated our spheroid culture system using non-small cell lung cancer H1650 cells. The spheroid formation and culture were observed by bright-field function of live cell imaging and fluorescence microscopy EMCCD, respectively. Spheroid size increased for 9 days and was sustained up to 30 days while the core region became dense (Supplementary Fig. S1A). Cell proliferation rate was significantly slower in spheroids than in monolayer culture system (doubling time of 3 and 1.5 days, respectively; Supplementary Fig. S1B). To determine whether there was a correlation between spheroid size and seeded cell number, different quantities of cells were seeded and the sizes of resulting spheroids were determined after 6-day incubation. Spheroid size and seeded cell number showed positive correlation (Supplementary Fig. S1C). The cells inside of the spheroids may become hypoxic due to their 3D structure (15). To monitor hypoxic conditions, we extracted proteins from spheroid cells and performed immunoblotting to detect the presence of hypoxia markers such as hypoxia-inducible factor-1 α (HIF1 α ; ref. 23) and HSP70 (24), as well as E-cadherin which mediates cell-cell contact (8). We found that the expression levels of these three proteins were significantly increased in spheroids. In the same condition, the levels of EGFR were decreased in 3D cells as expected (25) whereas those of GAPDH were unchanged (Supplementary Fig. S1D). We further confirmed hypoxic status by detecting the increase of HIF1 α and VEGF mRNA levels (Supplementary Fig. S1E).

To further investigate whether hypoxic conditions existed in the internal core region, we incubated spheroids grown for 5 days with a spheroid permeable hypoxia probe, LOX-1 (21) for 24 hours, and monitored the staining of LOX-1 by fluorescence microscopy. The LOX-1 signal was observed in spheroids but not in LOX-1 untreated and monolayer culture (Supplementary Fig. S1F). Despite hypoxic conditions, the internal structures of the cancer spheroids were populated with viable cells when the cells were checked after 6-day incubation (Supplementary Fig. S1G). These results demonstrate that the culture system used in this study generates typical cancer spheroids.

Park et al.

Morphologic classification and characteristics of cancer spheroids

Using this culture system, we examined 100 different human cancer cell lines (Fig. 1A) and classified them on the basis of spheroid morphology using bright-field function of fluorescence microscopy (Fig. 1B; Supplementary Table S1). The cancer cells (1,000 cells/well) became spheroids with the diameter from 200 to 1,000 μm after 6-day incubation. From the 100 tested cancer cell lines, we classified 91 cell lines into three distinct groups: round (R, 50 cases), mass (M, 14 cases), and aggregate-type (A, 27 cases; Fig. 1C). Nine cancer cell lines failed to form spheroids (N type). To monitor spheroid organization and cell–cell adhesion, we used F-actin staining as they are critical for cellular structure and tight junctions (26). The R-type cell lines generated round and compact spheroids with tight cell–cell adhesion, whereas the M-type cells formed the spheroids of unstructured outline with moderate cell–cell adhesion. The A-type cells showed a distinct aggregate-like morphology with weak cell–cell interactions (Fig. 1D). The

R- and M-type cells generated organized spheroids at early time, whereas the A-type cells showed disorganized aggregation (Supplementary Movies S1A–S1C).

To determine a relationship between cell proliferation rate and spheroid morphology, we compared the proliferation rates of three representative lung cancer cells (H226: R-type, H460: M-type, A549: A-type) between 2D and 3D culture systems. Although the growth rate of R-type H226 and M-type H460 cells were the lowest and highest in both culture systems, respectively, the growth rate of the A-type A549 cells was significantly reduced in 3D culture system (Fig. 1E; Supplementary Fig. S2A). As tight cell-to-cell interaction induces pericellular hypoxia (27), hypoxia status was determined to check the correlation between spheroid morphology and cell-to-cell interaction. We used LOX-1 staining to measure the hypoxia in the interiors of the 5-day cultured spheroids. Significantly higher LOX-1 staining was observed in the R-type spheroids compared with the two other types (Fig. 1F; Supplementary Fig. S2B). In the 2D culture system, none of the tested cancer cell lines displayed a hypoxia signal based on LOX-1

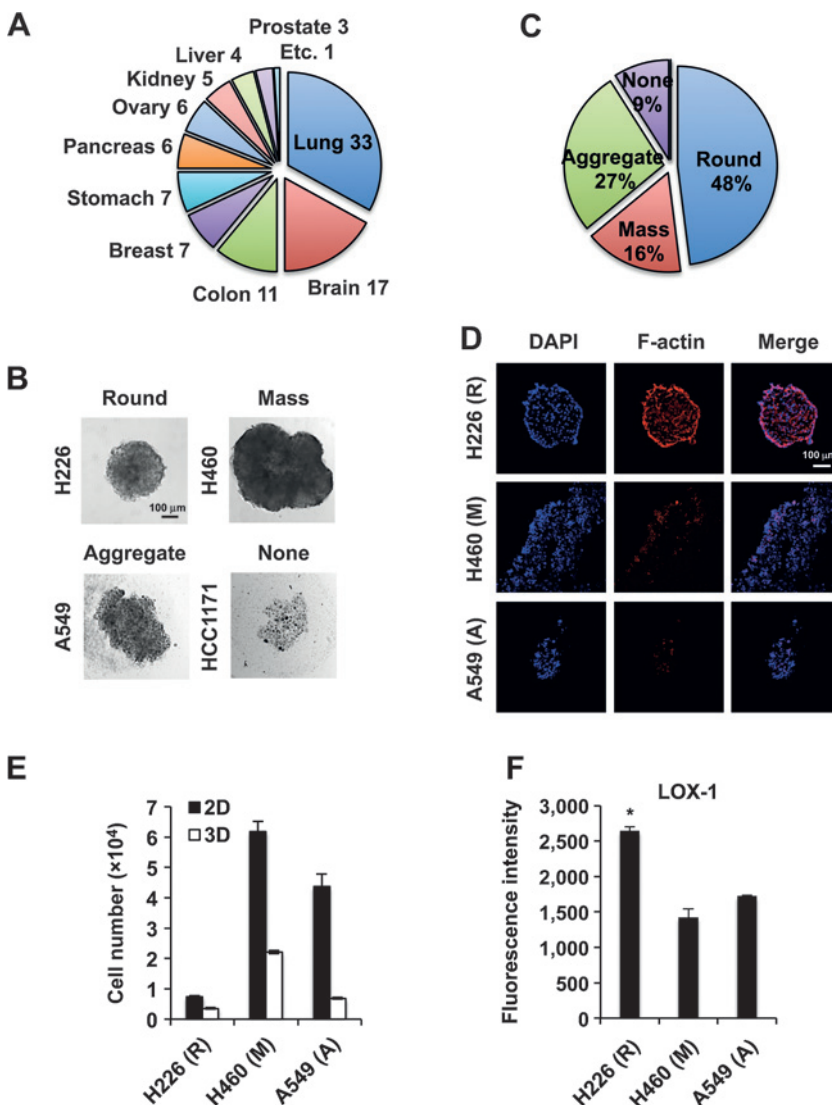


Figure 1.

Morphologic classification of cancer spheroids. A, cancer cell lines used for spheroid formation studies. B, the four representative (round, mass, aggregate type, and "none" spheroid formation) spheroid morphologies as shown by bright-field images of lung cancer spheroids after 6-day incubation in 3D culture. C, morphology distribution of the tested cancer cell lines. D, cell distribution and actin organization in spheroids. Nuclei and F-actin were stained with 4'-6 diamidino-2-phenylindole (DAPI) and phalloidin in 10- μm sectioned spheroids, respectively. E, growth comparison of the cancer cells with different morphologic types in 2D and 3D culture. The monolayer cells and spheroids (2,000 cells/well) were disrupted by cell detachment buffer and cell number was counted after 6-day cultivation. F, the hypoxic status of spheroids with different morphologic types. Each type of spheroid, cultured for 5 days in 3D plate, was incubated with 3D permeable hypoxia probe, LOX-1, for 24 hours and the mean fluorescence intensity was measured by fluorescence microscopy. *P* value was determined by one-way ANOVA. *, *P* < 0.01.

staining (Supplementary Fig. S2C). The two colon cancer cell lines, LoVo and SW480, formed the R- and A-type spheroids, respectively (Supplementary Fig. S2D). We detected elevated mRNA levels of *HIF1 α* and *VEGF* in the 3D spheroids compared with those in the 2D cultured LoVo, but not SW480, cells (Supplementary Fig. S2E and S2F). We further compared cell proliferation and hypoxia in the 2D and 3D systems of nine different cancer cell lines (lung cancer: H441, H23, Calu-6; colon cancer: LoVo, SW480, Colo205; GBM: LN18, U251MG, U251E4). The M-type (H23 and U251MG) and R-type spheroids (H441, LoVo, and LN18) showed the highest proliferation rate and hypoxia status, respectively (Supplementary Fig. S3A–S3C). These results suggest that the R-type spheroids generate hypoxic condition within their lumens due to tight cell–cell interaction.

We also measured drug permeability of spheroids as an independent indicator for the compactness of spheroids. Cell–cell interaction may form a diffusion barrier that would affect the delivery of anticancer drugs to the interiors of solid tumors (28, 29). Using three lung cancer cell lines (H226: R-type, H460: M-type, A549: A-type), which are representative of the different spheroid types, we compared the effective doses of four known antitumor drugs [5-fluorouracil (5-FU), SN-38, sorafenib, and 17-AAG] in 2D and 3D culture conditions. As 2D and 3D culture systems have different cell proliferation rates and structures, we used different conditions to determine drug sensitivity. In the 2D culture system, the cells were incubated with drugs for 1.5 days and the cell viability was monitored by lactate dehydrogenase (LDH) assay of the cell lysates. In this condition, all three tested cell lines showed similar drug sensitivity. Then, the cells were cultured in a 3D plate for 4 days and incubated with drugs for an additional 3 days and cell viability was determined as above. The spheroids of H226 cells showed higher resistance to all of the tested drugs compared with those of the two other cells (Table 1). To see whether this difference is generally applicable, we used an additional nine different cancer cell lines to compare drug sensitivity. Among the tested cell lines, the R-type spheroids (H441, LoVo, and LN18) showed higher resistance to drugs (Supplementary Fig. S3C). Thus, all the results suggest that the R-type spheroids would build up higher physical barrier to drugs due to tighter cell–cell adhesion.

Association of genetic profiles with spheroid morphology

To see whether the genetic characteristics of cell lines are related to spheroid morphology, we obtained gene expression, mutation, and copy number variation (CNV) data for the 70 tested cancer

cells (30, 11, 21, and 8 cell lines for R-, M-, A-, and N-types, respectively) from the database of Cancer Cell Line Encyclopedia (30). Among a total of 22,285 genes, we identified 2,202 genes that significantly [$P < 0.05$ for variable importance on the projection (VIP)] correlated with the four types of spheroids using multiblock partial least square-discriminant analysis (MPLS-DA). These 2,202 genes were then characterized by the mRNA abundance, mutations, and CNV, for 926, 65, and 1,333 genes, respectively (Supplementary Fig. S4A). Of these 2,202 genes, we focused on 560 genes that showed either high or low abundance of mRNA expression, mutations, and CNV (313, 32, and 229 genes, respectively; Supplementary Fig. S4A–S4D). The MPLS-DA model revealed that these signatures could stratify the 70 tested cancer cells into the four different types of spheroids (Fig. 2A) using six latent variables (LV; Supplementary Table S2), with a prediction accuracy of larger than 90% (Supplementary Fig. S4E) and misclassification error of less than 10%, during leave-one-out-cross-validations (Supplementary Fig. S4F). The block contribution in MPLS indicated that among the three types of molecular signatures, mRNA and CNV data significantly contributed to the ability of stratifying cancer cells into the different spheroid classes (Supplementary Fig. S4G). Although the genetic profiles are well separated by spheroid morphology, they are not always correlated with the results of pharmacodynamics (31) because the drug sensitivity can be varied depending on experimental conditions. To avoid the potential variation resulting from experimental conditions, we applied a different drug treatment condition that is adjusted to 2D and 3D culture systems but used the same cell viability assay.

We hypothesized that the molecular signatures for the 560 genes represent cellular processes or pathways crucial for the characteristics of the spheroids. Thus, we identified cellular processes significantly ($P < 0.1$) represented by the 560 signature genes by enrichment analysis of Gene Ontology Biological Processes (GOBP) using the DAVID software (32; Fig. 2B). The results showed that molecular signatures of the R-type spheroids were implicated in cellular processes relating to cell proliferation (regulation of cell proliferation and DNA replication) and defense response (T-cell receptor and JAK–STAT signaling). The M- and A-type spheroids were characterized by the MAPK pathway/DNA damage responses and by ion transport/neurologic process, respectively. We then reconstructed network models delineating these cellular processes, using only the genes showing spheroid-type specific molecular signatures. The network defined by the R-type spheroid signatures revealed high expression of mRNAs and CNV for cell surface molecules (*CD53* and *CD79B*), cytokine–cytokine receptors (*IL3/4/13*, *CSF2*, *IL3RA*, and *IL19A*), and secreted molecules (*F5*, *ADIPOR1*, *SPOCK2*, and *CMA1*), which activate JAK–STAT, T-cell receptor, small GTPase-mediated, and cell cycle-related signaling pathways and their downstream transcriptional regulators (Fig. 2C; Supplementary Fig. S5A). The network defined by the M-type spheroid signatures showed high expression of mRNA and CNV for molecules related to Integrin, Notch, and ERBB–MAPK signaling pathways, suggesting association with cytoskeleton organization and proliferation (Supplementary Fig. S5B). The network defined by A-type spheroid signatures showed high expression of mRNA and CNV in genes implicated with neurologic system-related processes such as *GRIN2D*, a neurotransmitter receptor, its downstream signaling pathway (*RGS12/16*, *GNAI3*, and *PTGS2*), and

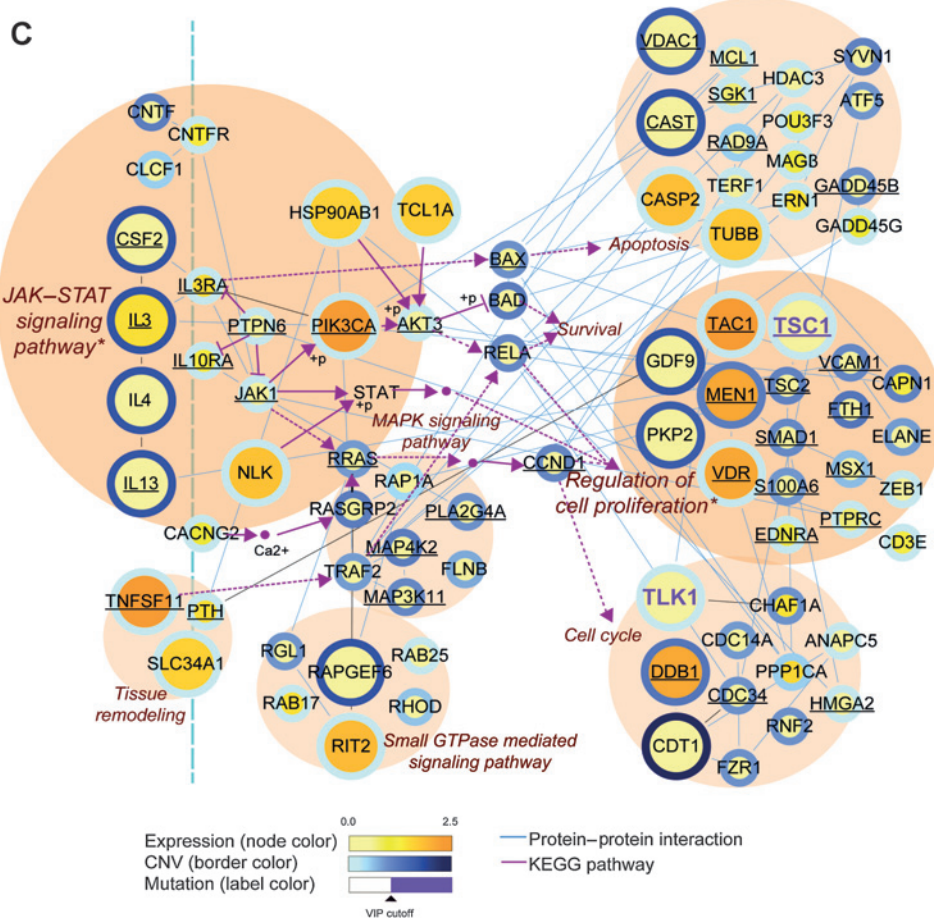
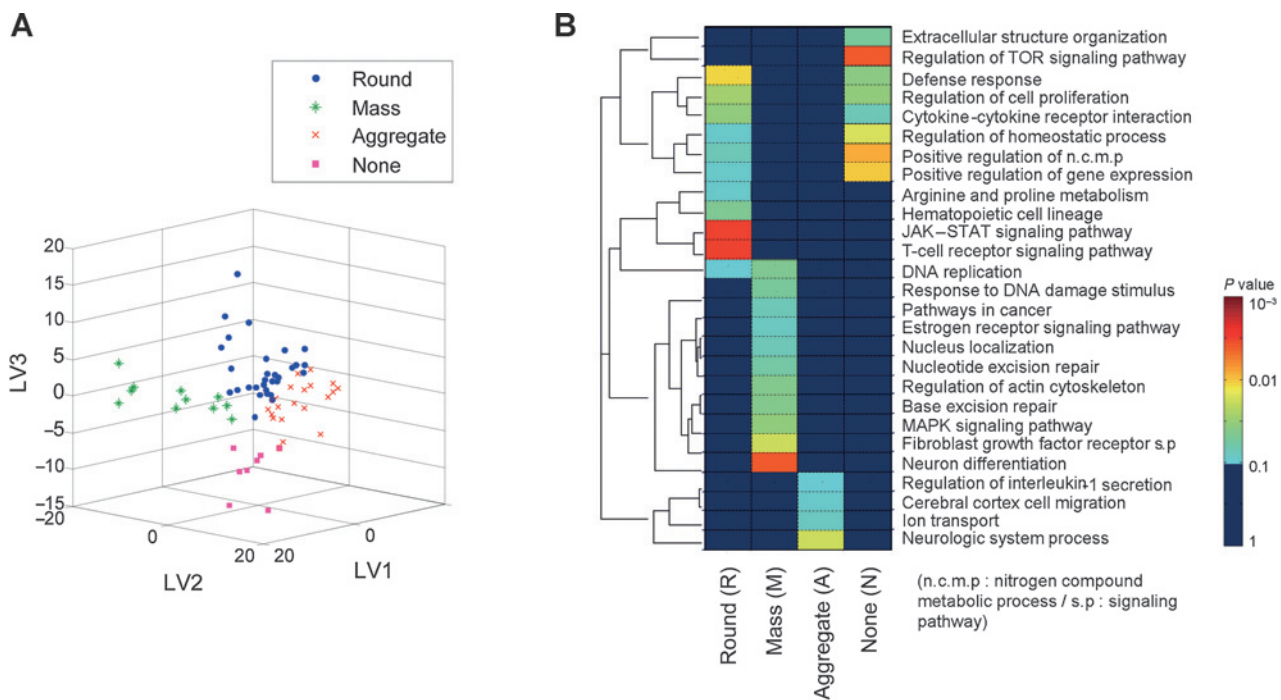
Table 1. The IC_{50} values of four different anticancer drugs (5-FU, SN-38, sorafenib, and 17-AAG) were determined in 2D and 3D cancer cells (H226, H460, and A549 lung cancer cell lines)

Drug	Culture condition	Cell line		
		H226 (R)	H460 (M)	A549 (A)
5-FU	2D	27 \pm 3	29 \pm 3	21 \pm 2
	3D	247 \pm 31 ^a	66 \pm 11	40 \pm 6
SN-38	2D	2 \pm 1	7 \pm 1	7 \pm 2
	3D	114 \pm 17 ^a	18 \pm 1	16 \pm 2
Sorafenib	2D	11 \pm 4	14 \pm 2	17 \pm 2
	3D	152 \pm 36 ^a	43 \pm 7	37 \pm 4
17-AAG	2D	11 \pm 2	19 \pm 2	9 \pm 2
	3D	149 \pm 32 ^a	29 \pm 1	28 \pm 6

NOTE: P values were determined by two-way ANOVA (spheroid type \times culture system).

^a $P < 0.01$.

Park et al.



CACNA16, a calcium transporter (Supplementary Fig. S5C). These networks suggest a set of cellular processes or signaling pathways that could be involved in determining spheroid morphology.

JAK-STAT pathway involved in round-type spheroid

We then investigated whether one of the signaling pathways suggested above would be functionally involved in spheroid morphology. We focused our attention to the JAK-STAT pathway, which was suggested as one of the signature pathways for R-type spheroids (Fig. 2C). Although STAT3 is known to enhance the antiapoptotic protein expression (33), prevent the cell-cycle arrest (34), and correlate with poor clinical prognosis (35, 36), it is not yet known whether STAT3 is involved in the physical characteristics of solid tumors. When we compared the expression and activation of STAT3 among the three cell lines representing different spheroid types, we found that total and phosphorylated STAT3 (T709) levels were higher in the R-type H226 cells than in the two other cell lines. In addition, the levels of cadherins and CD44, the membrane proteins for cell-cell interaction, were also higher in the R-type H226 cells (Fig. 3A). To test whether the inhibition of STAT3 would change the morphology of the R-type spheroids, we treated the R-type H226 and H441 cells with AG490, a JAK2-specific inhibitor, and monitored changes in spheroid morphology. After 3-day incubation with AG490, the outer layers of the spheroids were loosened (Supplementary Fig. S6A), and their lumens showed reduced hypoxic condition (Fig. 3B). The AG490-treated spheroids of H226 cells also decreased the levels of cadherins and CD44 as well as the phosphorylation levels of STAT3 (Fig. 3C).

As the R-type spheroids showed higher resistance to anticancer drugs, we tested whether AG490 treatment would enhance anticancer drug sensitivity by improving drug penetration. First, we monitored the significance of the JAK-STAT pathway in drug penetration using bimolecular fluorescence complementation (BiFC) system that detects the rapamycin-induced interaction between FKBP12 and FRB domain of mTOR (37, 38). We fused complementary fragments of Venus fluorescence protein to the C-terminal ends of FKBP12 and FRB. Rapamycin-induced association between FKBP12 and FRB would be detected by restoration of functional Venus fluorescence. The fluorescence intensity resulting from the rapamycin-dependent association of the two fusion proteins was increased in the spheroids treated with AG490 and rapamycin (Fig. 3D; Supplementary Fig. S6B and S6C). As the effect of rapamycin is usually indicated by the phosphorylation of S6K, we also monitored whether S6K phosphorylation is affected by AG490 treatment. The cotreatment of AG490 and rapamycin significantly reduced phosphorylation of S6K (Supplementary Fig. S6D). Second, we directly measured drug penetration in spheroids by LC/MS-MS analysis as previously described (39),

using 17-AAG as a testing drug as it showed unique peak in LC/MS-MS analysis. After 2-day preincubation with AG490, we treated H226 spheroids with 17-AAG for 5 hours. The concentration of 17-AAG in the spheroids was increased 2.2-fold by AG490 treatment (Fig. 3E).

To determine the significance of the JAK-STAT pathway for tumor permeability, we treated H226 spheroids with 5-FU and 17-AAG (showing weak cytotoxicity in R-type spheroids; see Table 1) alone or in combination with AG490, and examined how AG490 treatment affects the cytotoxicity of the two drugs. The treatment of 5-FU and 17-AAG with AG490 enhanced the cell death to 43% and 54%, respectively, whereas 5-FU and 17-AAG alone induced the cell death to 10% and 15%, respectively (Fig. 3F). Although the inhibition of STAT3 itself might induce autophagy-mediated cell death that could also reduce the permeability barrier (40), cell death was not observed with STAT3 inhibition in our culture system. Taken together, these data suggest the importance of the JAK-STAT pathway for determination of the R-type spheroids and tumor permeability.

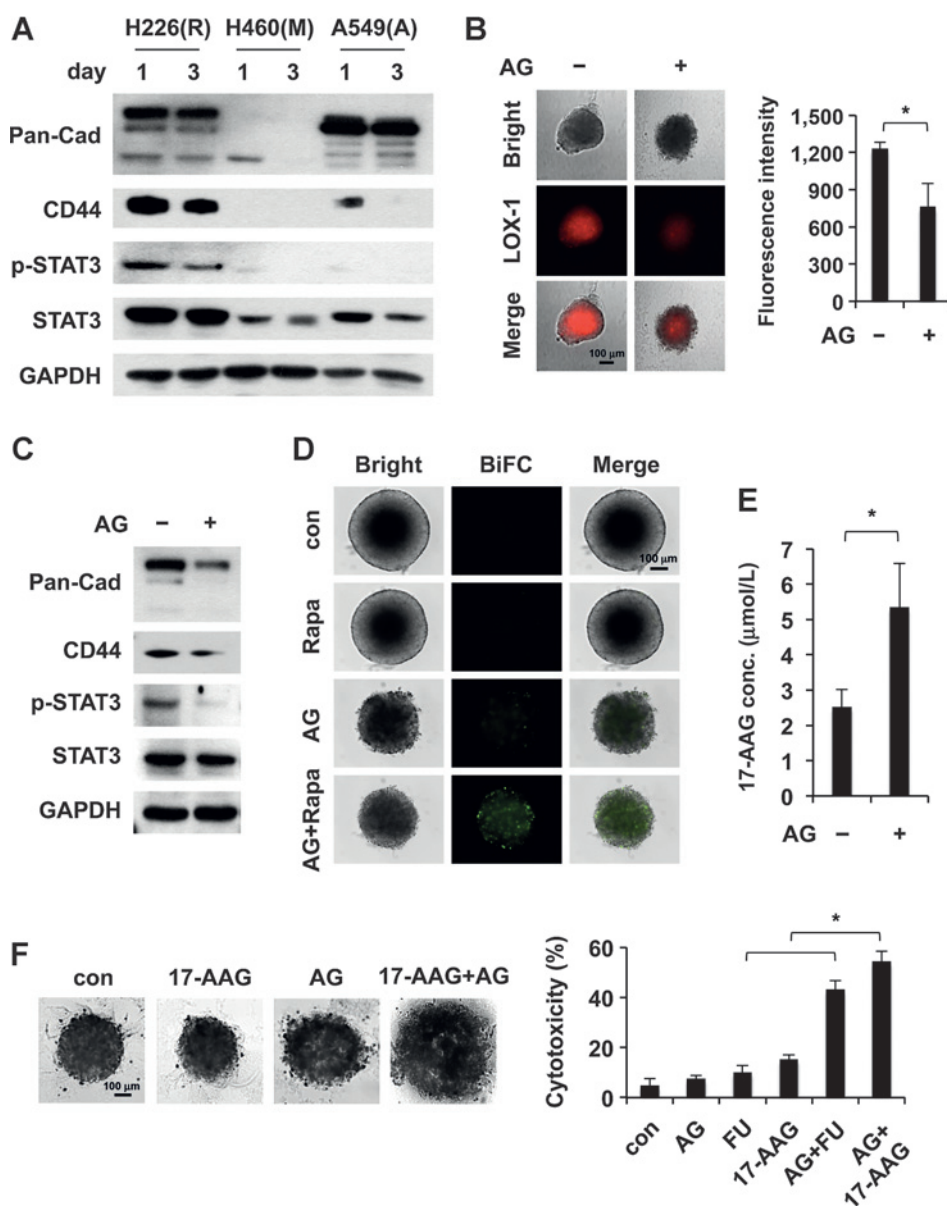
Validation of JAK-STAT pathway in drug sensitivity of patient-derived spheroids

To further validate our analysis, we obtained primary cells from 9 different GBM patients that were previously reported (19, 20), and classified them on the basis of spheroid morphology. The patient-derived cells also formed one of the three different spheroid morphology types (Fig. 4A, the numbers represent patients' identification). We analyzed gene expression and CNV data from these cells and identified 1,831 genes that significantly ($P < 0.05$ for VIP) correlated with the four types of spheroids using MPLS in mRNA abundance and CNV (for 1,572 and 301 genes, respectively). Among the 186 genes with the R type-specific molecular signatures (Supplementary Fig. S4A), 36 genes showed mRNA abundance and CNV that strongly correlated with the GBM patient-derived R-type spheroids (Supplementary Fig. S7A and S7B) and could further distinguish different types of spheroids (Fig. 4B). We then examined the relationships between the 36 genes and the JAK-STAT signature (7 R type-specific genes related to JAK-STAT pathway) from cell lines. To this end, we identified the overlapping genes between the two gene sets and then evaluated the significance of the overlapping genes using the hypergeometric test. The 36 genes and their interactors included 2 and 6 of the 7 genes related to the JAK-STAT pathway, respectively ($P = 1.13 \times 10^{-2}$ and 4.06×10^{-5} ; Supplementary Fig. S7C). Second, overlaying the 36 genes onto the JAK-STAT pathway in the R type-specific network (Fig. 2C) revealed the two overlapping genes (*IL3* and *IL13*), the links of 12 genes related to the JAK-STAT pathway in the R type-specific network to 7 (*IL3*, *IL13*, *CCNI2*, *TUBB*, *HDAC9*, *SLC22A4*, and *CASP2*) of the 36 genes from patient-derived R-type spheroids, and finally the involvement of 5 of the

Figure 2.

Molecular signatures associated with different spheroid morphology groups. A, separation of different spheroid subtypes by MPLS-DA using 560 discriminatory genes. The separation was displayed in a 3D latent space (LV1-3 obtained by PLS-DA). B, GOBPs and Kyoto Encyclopedia of Genes and Genomes (KEGG) pathways represented by 186 (R), 158 (M), 152 (A), and 176 (N) subtype-specific discriminatory genes. The color represents $-\log_{10}(P)$, where P is the enrichment P value obtained from DAVID functional enrichment tool. C, a subnetwork describing cellular processes associated with JAK-STAT pathway in the round-type spheroid. The nodes are arranged so that those with the same GOBPs or KEGG pathways are grouped together. *, GOBPs or KEGG pathways overrepresented by the 186 round type-specific genes. Node, border, and label colors represent VIPs computed from PLS-DA using mRNA expression, CNVs and mutation, respectively. The 186 R type-specific genes were denoted by large nodes. Underlined node labels represent cancer drug targets reported in NCI chemical index. Blue edges represent protein-protein interactions selected from HotNet and obtained from the databases with experimental evidence (HitPredict, STRING, and GeneGO). Purple edges denote signaling pathways obtained from KEGG pathway database.

Park et al.

**Figure 3.**

JAK-STAT pathway implicated in round-type spheroid morphology. A, levels of indicated proteins were compared among different morphology groups by Western blotting at the indicated time points. Pan-Cad indicates Western blot analysis with pan-cadherin antibody. Activation of STAT3 was determined using p-STAT3 (T705) antibody. B, hypoxic status of H226 cell-derived spheroids (R type) indicated by LOX-1 staining. The spheroids of H226 cells were treated with or without AG490 (JAK2 inhibitor, 150 $\mu\text{mol/L}$) for 2 days and LOX-1 was added for fluorescence staining (left). The mean fluorescence intensity was represented by bar graph (right). C, the effect of AG490 on cellular levels of the indicated proteins was determined by Western blotting as above. H226 cell spheroids were incubated with or without AG490 for 2 days. D, BiFC vectors (VN-FKBP12 and VC-FRB) were coexpressed in 2D-cultured 293T cells and 5,000 cells were seeded to generate spheroids. After 3-day incubation, spheroids were incubated in the absence or presence of AG490 for 2 days. Rapamycin (1 $\mu\text{mol/L}$) was added to induce green fluorescence signal from BiFC. E, after 2-day preincubation with AG490, H226 cell-derived spheroids were treated with 17-AAG (125 $\mu\text{mol/L}$) for 5 hours. 17-AAG concentration in the spheroids was determined by LC/MS-MS method. F, the significance of the JAK-STAT pathway for drug resistance. H226 cell-derived spheroids were incubated in the absence or presence of AG490. After 2 days, the spheroids were further incubated with 5-FU (125 $\mu\text{mol/L}$) or 17-AAG (125 $\mu\text{mol/L}$) for 3 days. Bright-field images were taken after the indicated drug treatment and the LDH activity was determined to check cytotoxicity. *P* value was determined by Student *t* test. *, *P* < 0.01. con, control.

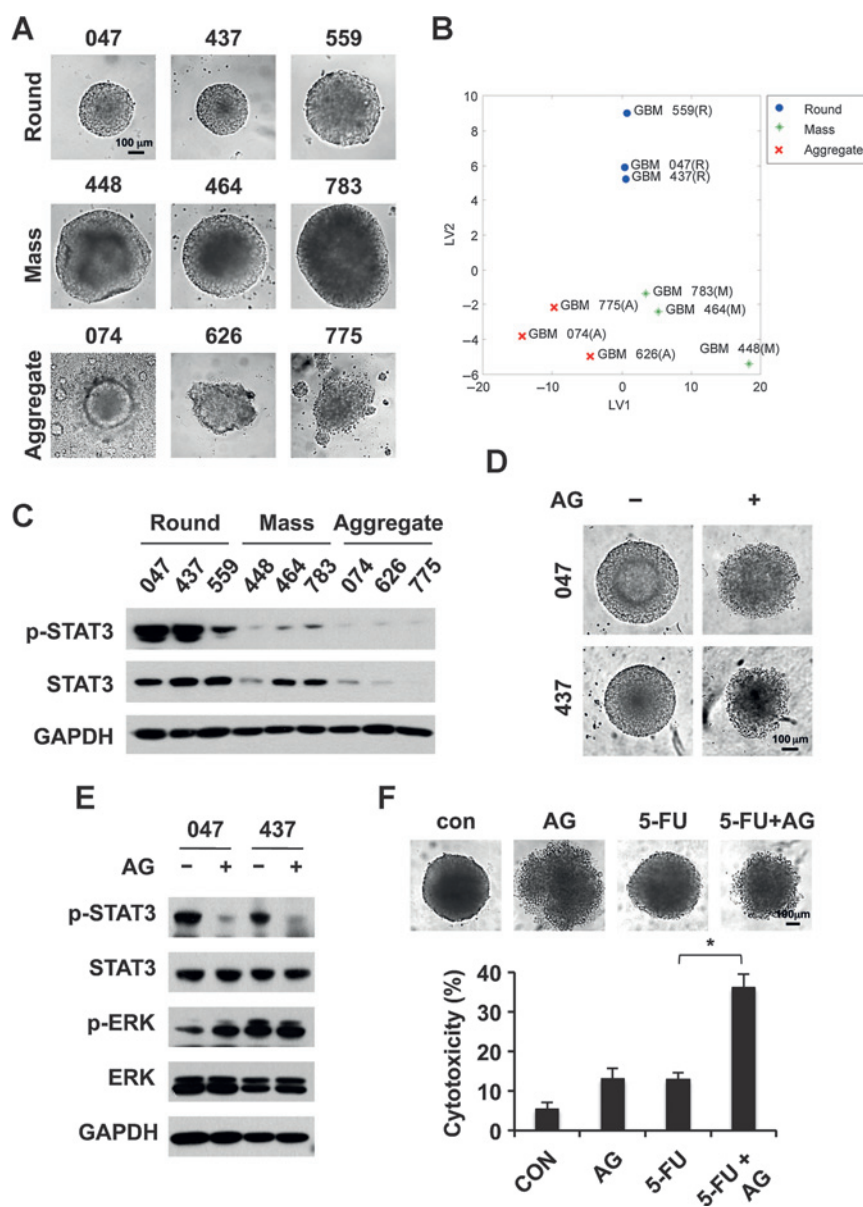
36 genes in the downstream target genes of JAK-STAT pathway including *TNFSF11*, *PATZ1*, *WDR6*, *CDT1*, and *TLK1* (Supplementary Fig. S7D). All these data suggest that the 36-gene signature from patient-derived R-type spheroids was closely linked to JAK-STAT signature identified from the cell lines. To confirm this possibility, we determined the activation of STAT3 among different patient-derived cancer cells and found that STAT3 was highly activated in the R-type GBM spheroids (Fig. 4C). When we treated these spheroids with AG490, the R-type morphology was changed to a more loose structure (Fig. 4D) with the decrease of phosphorylated STAT3 (Fig. 4E). To see whether the inhibition of STAT3 would sensitize the cancer cells to 5-FU, we treated the O47 cancer cells with either 5-FU or AG490 or both, and monitored cell death. We found that the cytotoxicity of 5-FU was greatly enhanced by the combined treatment with AG490 (Fig. 4F).

In vivo validation of JAK-STAT pathway in drug sensitivity

The significance of the JAK-STAT pathway in drug sensitivity of tumors was also tested in mouse xenograft model using H1650 cells that forms R-type spheroids with hyperactivated STAT3 and shows drug resistance *in vivo* (41). The mice were treated with 5-FU or AG490 alone, and 5-FU plus AG490 as described in Materials and Methods, and their effect on tumor growth was monitored. Treatment with 5-FU suppressed tumor growth, whereas AG490 had little effect (Fig. 5A). Combination of 5-FU with AG490 further reduced tumor growth. None of these treatments influenced body weight (Supplementary Fig. S8A). When tumor weights were compared after sacrificing the mice, similar results were obtained (Fig. 5B and Supplementary Fig. S8B). The effect of chemicals on cell-cell adhesion was examined by Western blotting with cell adhesion markers such as EpCAM and E-cadherin.

Figure 4.

JAK-STAT pathway for spheroid morphology and drug sensitivity of patient-derived cancer cells. A, morphologies of nine GBM patient-derived spheroids. The bright-field images of the spheroids were grouped on the basis of morphologic types. The numbers indicate patient identification. B, separation of different spheroid subtypes by PLS-DA using the 36 discriminatory genes. The separation was displayed in 2D latent space (LV1-2 obtained by PLS-DA). C, the status of STAT3 activation in the patient cell-derived spheroids. Levels of total and phosphorylated STAT3 were compared among different spheroid groups by Western blotting. D, the effect of STAT3 inhibition on the round-type spheroids. The spheroids were incubated in the absence or presence of AG490 (150 $\mu\text{mol/L}$) as above and the change of the morphology was monitored by microscopy. E, the effect of AG490 on the activation of STAT3 was determined by Western blot analysis. F, the effect of STAT3 inhibition on drug sensitivity. The GBM patient-derived spheroids were incubated in the absence or presence of AG490 for 2 days. The spheroids were further incubated with 5-FU (125 $\mu\text{mol/L}$) for 3 days, and morphology change and cytotoxicity were determined by bright field of fluorescence microscopy and the LDH activity, respectively. *P* value was determined by Student *t* test. *, *P* < 0.01. con, control.



Both markers were significantly suppressed by the combined treatment of AG490 and 5-FU in two independent samples (Fig. 5C). We also compared cell death of the isolated tumor tissues using TUNEL staining and found significantly increased apoptosis in the tumor tissues treated with 5-FU and AG490 (Fig. 5D). The histologic analysis also showed that the tumors treated with AG490 and 5-FU showed significantly loosened tissue structure (Fig. 5E).

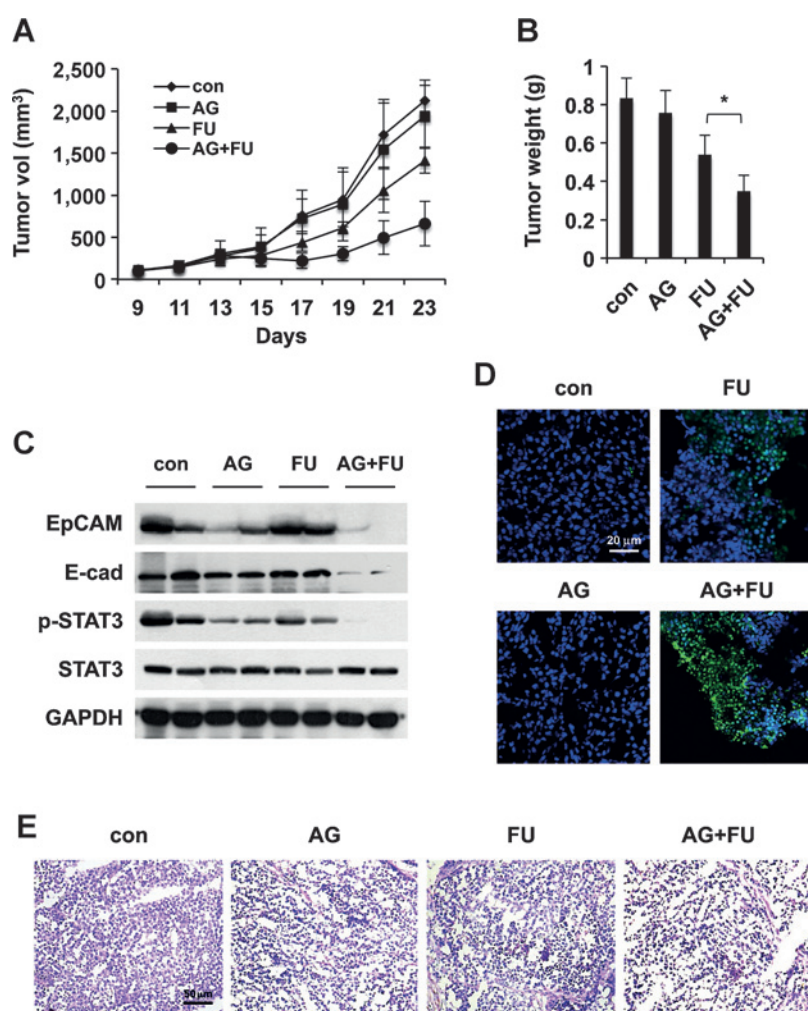
Discussion

This work demonstrates that 100 different cancer cells could be classified into four distinct 3D morphology types, suggesting that the analysis of spheroid morphology could be a simple but reliable way to predict tumor permeability. However, considering genetic heterogeneity within each morphology type, genetic anal-

ysis of cancer cells might be necessary to identify the signaling pathways contributing to specific morphology. The permeability barrier provides a condition to induce intratumoral heterogeneity of cancer cells as the cells would have different microenvironments for nutrition and oxygen availability. For instance, cells in the inner core of tumors with tight cell-cell adhesions would face hypoxia and nutrition shortage due to high diffusion barrier of external cells (3, 29). Meanwhile, these cells may acquire mutations or epigenetic changes allowing them to survive these harsh conditions (2, 42).

In our experiments, spheroid morphology did not show tissue dependency, suggesting that genes involved in tissue differentiation would not be the predominant determinants for spheroid morphology. Systematic analysis of the genetic profiles suggested the group of genes distinct for the four different types of spheroids. Among the four types of tumor spheroids, the round type showed

Park et al.

**Figure 5.**

In vivo validation of JAK-STAT pathway for drug sensitivity. H1650 cells were subcutaneously injected into the flank of 8-week-old BALB/c nude mice. The mice ($n = 6$ per each group) were treated with saline or 5-FU (10 mg/kg) with or without AG490 (5 mg/kg) as described in Materials and Methods. A, the effect of chemicals on tumor volume that was measured every 2 days. B, after sacrificing the mice, tumors were isolated and their weights were measured. P value was determined by Student t test. *, $P < 0.01$. C, the levels of phosphorylated STAT3 and adhesion markers (EpCAM and E-cadherin) were compared by Western blot analysis. D, apoptosis in the tumor tissues was determined by TUNEL assay (green fluorescence). Nuclei were stain with DAPI (blue). E, hematoxylin and eosin staining of the tumor tissues isolated from each group. con, control.

the most compact structure with the highest degree of drug resistance. They showed unique genetic signatures including the JAK-STAT signaling pathway. In this context, STAT3 activates the NF- κ B pathway through direct interaction with RELA in the nucleus of cancer cells, leading to the enhancement of cell proliferation, survival, and invasion (43). Constitutively, active STAT3 has been observed in a variety of human cancers (44). Besides, it has been shown to upregulate EpCAM and CD44, the membrane proteins associated with cell-cell adhesion (45), implying a potential role of STAT3 in the determination of tumor structure and morphology. We found that inhibition of STAT3 rendered the round type more permeable to drug penetration, supporting the functional significance of STAT3 in tumor permeability although the causal relationship of STAT3 to the determination of tumor permeability is not completely clear at this moment. STAT3 is also known to confer resistance against hypoxia (43). As the round-type spheroids would generate hypoxic conditions due to the compact adhesion of the cells, the activation of STAT3 would be helpful for the survival of the cancer cells under hypoxic conditions. In monolayer cell conditions, the potential ability to mediate the physical properties of tumors cannot be easily detected. Therefore, combined analysis of tumor spheroids with genetic profiles can help to identify new therapeutic targets,

and also to understand the physical context of known targets in an environment simulating different tumor types.

Morphologic analysis of tumor spheroids can also be explored for clinical application and drug discovery. Much effort has been invested to understand the molecular mechanisms underlying the resistance of tumors to anticancer drugs. One well-known form of resistance is to extrude drugs from cells by plasma membrane-transport proteins (46). For drug resistance that falls outside of this category, tumors can become resistant as a consequence of mutations of genes encoding intracellular targets and affecting associated pathways. These mutations can affect the drug-target interactions or induce compensatory pathways (47). Another potential mechanism for drug resistance that is more relevant to this study is the permeability barrier to drugs. Although many key mediators in cell proliferation and death have been intensively tested for therapeutic potential, the factors implicated for the physical properties of solid tumors are less explored. To design an effective therapeutic strategy, the physical environment of the tumor structure should also be taken into account. Combined analysis of spheroid morphology and genetic profiles could be an effective way to discover new therapeutic targets and to design an efficient therapeutic strategy for cancer patients.

Disclosure of Potential Conflicts of Interest

No potential conflicts of interest were disclosed.

Authors' Contributions

Conception and design: M.C. Park, S. Kim

Development of methodology: M.C. Park, S.H. Son, Y.H. Kim

Acquisition of data (provided animals, acquired and managed patients, provided facilities, etc.): M.C. Park, S.H. Son, Y.H. Kim, D. Han, T. Kang, S.H. Paek, H.J. Seol, D.-H. Nam

Analysis and interpretation of data (e.g., statistical analysis, biostatistics, computational analysis): M.C. Park, H. Jeong, S.H. Son, H.E. Moon, D. Hwang, S. Kim

Writing, review, and/or revision of the manuscript: M.C. Park, N.H. Kwon, D. Hwang, S. Kim

Administrative, technical, or material support (i.e., reporting or organizing data, constructing databases): M.C. Park, T. Kang, S.H. Paek, D. Hwang, H.J. Seol, S. Kim

Study supervision: S.H. Paek, S. Kim

Acknowledgments

The authors thank Hoi Kyoung Kim for the microscopy operating and Dr. Jung Won Lee for his advice.

Grant Support

This work was supported by the Global Frontier Project (NRF-M3A6A4-2010-0029785; to S. Kim) of the National Research Foundation funded by the Ministry of Science, ICT & Future Planning (MSIP) of Korea. This work was also supported by the Gyeonggi Research Development Program and the Ministry of Health & Welfare (HI13C21480301; to S. Kim).

The costs of publication of this article were defrayed in part by the payment of page charges. This article must therefore be hereby marked *advertisement* in accordance with 18 U.S.C. Section 1734 solely to indicate this fact.

Received September 3, 2014; revised November 19, 2015; accepted December 7, 2015; published OnlineFirst December 16, 2015.

References

- Vaupel P, Kallinowski F, Okunieff P. Blood flow, oxygen and nutrient supply, and metabolic microenvironment of human tumors: a review. *Cancer Res* 1989;49:6449–65.
- Gatenby RA, Gillies RJ. Why do cancers have high aerobic glycolysis? *Nat Rev Cancer* 2004;4:891–9.
- Tredan O, Galmarini CM, Patel K, Tannock IF. Drug resistance and the solid tumor microenvironment. *J Natl Cancer Inst* 2007;99:1441–54.
- Shain KH, Dalton WS. Cell adhesion is a key determinant in de novo multidrug resistance (MDR): new targets for the prevention of acquired MDR. *Mol Cancer Ther* 2001;1:69–78.
- Weaver VM, Lelievre S, Lakins JN, Chrenek MA, Jones JC, Giancotti F, et al. beta4 integrin-dependent formation of polarized three-dimensional architecture confers resistance to apoptosis in normal and malignant mammary epithelium. *Cancer Cell* 2002;2:205–16.
- Kim JB. Three-dimensional tissue culture models in cancer biology. *Semin Cancer Biol* 2005;15:365–77.
- Anderson AR, Weaver AM, Cummings PT, Quaranta V. Tumor morphology and phenotypic evolution driven by selective pressure from the microenvironment. *Cell* 2006;127:905–15.
- Takeichi M. Cadherin cell adhesion receptors as a morphogenetic regulator. *Science* 1991;251:1451–5.
- Miranti CK, Brugge JS. Sensing the environment: a historical perspective on integrin signal transduction. *Nat Cell Biol* 2002;4:E83–90.
- Friedl P, Alexander S. Cancer invasion and the microenvironment: plasticity and reciprocity. *Cell* 2011;147:992–1009.
- Debnath J, Brugge JS. Modelling glandular epithelial cancers in three-dimensional cultures. *Nat Rev Cancer* 2005;5:675–88.
- Sutherland RM. Cell and environment interactions in tumor microregions: the multicell spheroid model. *Science* 1988;240:177–84.
- Shweiki D, Neeman M, Itin A, Keshet E. Induction of vascular endothelial growth factor expression by hypoxia and by glucose deficiency in multicell spheroids: implications for tumor angiogenesis. *Proc Natl Acad Sci U S A* 1995;92:768–72.
- Curcio E, Salerno S, Barbieri G, De Bartolo L, Drioli E, Bader A. Mass transfer and metabolic reactions in hepatocyte spheroids cultured in rotating wall gas-permeable membrane system. *Biomaterials* 2007;28:5487–97.
- Hirschhaeuser F, Menne H, Dittfeld C, West J, Mueller-Klieser W, Kunz-Schughart LA. Multicellular tumor spheroids: an underestimated tool is catching up again. *J Biotechnol* 2010;148:3–15.
- Freyer JP, Sutherland RM. Proliferative and clonogenic heterogeneity of cells from EMT6/Ro multicellular spheroids induced by the glucose and oxygen supply. *Cancer Res* 1986;46:3513–20.
- Bates RC, Edwards NS, Yates JD. Spheroids and cell survival. *Crit Rev Oncol Hematol* 2000;36:61–74.
- Kunz-Schughart LA, Kreutz M, Knuechel R. Multicellular spheroids: a three-dimensional *in vitro* culture system to study tumour biology. *Int J Exp Pathol* 1998;79:1–23.
- Oh YT, Cho HJ, Kim J, Lee JH, Rho K, Seo YJ, et al. Translational validation of personalized treatment strategy based on genetic characteristics of glioblastoma. *PLoS One* 2014;9:e103327.
- Joo KM, Kim J, Jin J, Kim M, Seol HJ, Muradov J, et al. Patient-specific orthotopic glioblastoma xenograft models recapitulate the histopathology and biology of human glioblastomas in situ. *Cell Rep* 2013;3:260–73.
- Zhang S, Hosaka M, Yoshihara T, Negishi K, Iida Y, Tobita S, et al. Phosphorescent light-emitting iridium complexes serve as a hypoxia-sensing probe for tumor imaging in living animals. *Cancer Res* 2010;70:4490–8.
- Eiraku M, Takata N, Ishibashi H, Kawada M, Sakakura E, Okuda S, et al. Self-organizing optic-cup morphogenesis in three-dimensional culture. *Nature* 2011;472:51–6.
- Wang GL, Jiang BH, Rue EA, Semenza GL. Hypoxia-inducible factor 1 is a basic-helix-loop-helix-PAS heterodimer regulated by cellular O₂ tension. *Proc Natl Acad Sci U S A* 1995;92:5510–4.
- Iwaki K, Chi SH, Dillmann WH, Mestrlil R. Induction of HSP70 in cultured rat neonatal cardiomyocytes by hypoxia and metabolic stress. *Circulation* 1993;87:2023–32.
- Luca AC, Mersch S, Deenen R, Schmidt S, Messner I, Schafer KL, et al. Impact of the 3D microenvironment on phenotype, gene expression, and EGFR inhibition of colorectal cancer cell lines. *PLoS One* 2013;8:e59689.
- Madara JL. Tight junction dynamics: is paracellular transport regulated? *Cell* 1988;53:497–8.
- Sheta EA, Trout H, Gildea JJ, Harding MA, Theodorescu D. Cell density mediated pericellular hypoxia leads to induction of HIF-1alpha via nitric oxide and Ras/MAP kinase mediated signaling pathways. *Oncogene* 2001;20:7624–34.
- Watton SJ, Downward J. Akt/PKB localisation and 3' phosphoinositide generation at sites of epithelial cell-matrix and cell-cell interaction. *Curr Biol* 1999;9:433–6.
- Minchinton AJ, Tannock IF. Drug penetration in solid tumours. *Nat Rev Cancer* 2006;6:583–92.
- Barretina J, Caponigro G, Stransky N, Venkatesan K, Margolin AA, Kim S, et al. The Cancer Cell Line Encyclopedia enables predictive modelling of anticancer drug sensitivity. *Nature* 2012;483:603–7.
- Haibe-Kains B, El-Hachem N, Birbak NJ, Jin AC, Beck AH, Aerts HJ, et al. Inconsistency in large pharmacogenomic studies. *Nature* 2013;504:389–93.
- Huang da W, Sherman BT, Lempicki RA. Systematic and integrative analysis of large gene lists using DAVID bioinformatics resources. *Nat Protoc* 2009;4:44–57.
- Mora LB, Buettner R, Seigne J, Diaz J, Ahmad N, Garcia R, et al. Constitutive activation of Stat3 in human prostate tumors and cell lines: direct inhibition of Stat3 signaling induces apoptosis of prostate cancer cells. *Cancer Res* 2002;62:6659–66.

Park et al.

34. Xiong H, Zhang ZG, Tian XQ, Sun DF, Liang QC, Zhang YJ, et al. Inhibition of JAK1, 2/STAT3 signaling induces apoptosis, cell cycle arrest, and reduces tumor cell invasion in colorectal cancer cells. *Neoplasia* 2008;10:287–97.
35. Kusaba T, Nakayama T, Yamazumi K, Yakata Y, Yoshizaki A, Inoue K, et al. Activation of STAT3 is a marker of poor prognosis in human colorectal cancer. *Oncol Rep* 2006;15:1445–51.
36. Yu H, Jove R. The STATs of cancer—new molecular targets come of age. *Nat Rev Cancer* 2004;4:97–105.
37. Shyu YJ, Suarez CD, Hu CD. Visualization of ternary complexes in living cells by using a BiFC-based FRET assay. *Nat Protoc* 2008;3:1693–702.
38. Raught B, Gingras AC, Sonenberg N. The target of rapamycin (TOR) proteins. *Proc Natl Acad Sci U S A* 2001;98:7037–44.
39. Lee JB, Son SH, Park MC, Kim TH, Kim MG, Yoo SD, et al. A novel *in vitro* permeability assay using three-dimensional cell culture system. *J Biotechnol* 2015;205:93–100.
40. You L, Wang Z, Li H, Shou J, Jing Z, Xie J, et al. The role of STAT3 in autophagy. *Autophagy* 2015;11:729–39.
41. Okamoto K, Okamoto I, Hatashita E, Kuwata K, Yamaguchi H, Kita A, et al. Overcoming erlotinib resistance in EGFR mutation-positive non-small cell lung cancer cells by targeting survivin. *Mol Cancer Ther* 2012;11:204–13.
42. Gillies RJ, Gatenby RA. Hypoxia and adaptive landscapes in the evolution of carcinogenesis. *Cancer Metastasis Rev* 2007;26:311–7.
43. Yu H, Pardoll D, Jove R. STATs in cancer inflammation and immunity: a leading role for STAT3. *Nat Rev Cancer* 2009;9:798–809.
44. Barre B, Vigneron A, Perkins N, Roninson IB, Gamelin E, Coqueret O. The STAT3 oncogene as a predictive marker of drug resistance. *Trends Mol Med* 2007;13:4–11.
45. Visvader JE, Lindeman GJ. Cancer stem cells: current status and evolving complexities. *Cell Stem Cell* 2012;10:717–28.
46. Gottesman MM, Fojo T, Bates SE. Multidrug resistance in cancer: role of ATP-dependent transporters. *Nat Rev Cancer* 2002;2:48–58.
47. Yun CH, Mengwasser KE, Toms AV, Woo MS, Greulich H, Wong KK, et al. The T790M mutation in EGFR kinase causes drug resistance by increasing the affinity for ATP. *Proc Natl Acad Sci U S A* 2008;105:2070–5.

Cancer Research

The Journal of Cancer Research (1916–1930) | The American Journal of Cancer (1931–1940)

Novel Morphologic and Genetic Analysis of Cancer Cells in a 3D Microenvironment Identifies STAT3 as a Regulator of Tumor Permeability Barrier Function

Min Chul Park, Hyobin Jeong, Sung Hwa Son, et al.

Cancer Res 2016;76:1044-1054. Published OnlineFirst December 16, 2015.

Updated version	Access the most recent version of this article at: doi: 10.1158/0008-5472.CAN-14-2611
Supplementary Material	Access the most recent supplemental material at: http://cancerres.aacrjournals.org/content/suppl/2015/12/15/0008-5472.CAN-14-2611.DC1.html

Cited articles	This article cites 47 articles, 14 of which you can access for free at: http://cancerres.aacrjournals.org/content/76/5/1044.full.html#ref-list-1
-----------------------	--

E-mail alerts	Sign up to receive free email-alerts related to this article or journal.
Reprints and Subscriptions	To order reprints of this article or to subscribe to the journal, contact the AACR Publications Department at pubs@aacr.org .
Permissions	To request permission to re-use all or part of this article, contact the AACR Publications Department at permissions@aacr.org .